

Quantitative determination of chromophore concentrations from 2D photoacoustic images using a nonlinear model-based inversion scheme

Jan Laufer,* Ben Cox, Edward Zhang, and Paul Beard

Department of Medical Physics & Bioengineering, University College London,
Malet Place Engineering Building, London WC1E 6BT, UK

*Corresponding author: jlaufer@medphys.ucl.ac.uk

Received 30 April 2009; revised 11 December 2009; accepted 19 December 2009;
posted 21 January 2010 (Doc. ID 110791); published 3 March 2010

A model-based inversion scheme was used to determine absolute chromophore concentrations from multiwavelength photoacoustic images. The inversion scheme incorporated a forward model, which predicted 2D images of the initial pressure distribution as a function of the spatial distribution of the chromophore concentrations. It comprised a multiwavelength diffusion based model of the light transport, a model of acoustic propagation and detection, and an image reconstruction algorithm. The model was inverted by fitting its output to measured photoacoustic images to determine the chromophore concentrations. The scheme was validated using images acquired in a tissue phantom at wavelengths between 590 nm and 980 nm. The phantom comprised a scattering emulsion in which up to four tubes, filled with absorbing solutions of copper and nickel chloride at different concentration ratios, were submerged. Photoacoustic signals were detected along a line perpendicular to the tubes from which images of the initial pressure distribution were reconstructed. By varying the excitation wavelength, sets of multiwavelength photoacoustic images were obtained. The majority of the determined chromophore concentrations were within $\pm 15\%$ of the true value, while the concentration ratios were determined with an average accuracy of -1.2% . © 2010 Optical Society of America

OCIS codes: 170.5120, 300.0300, 100.3190.

1. Introduction

Biomedical photoacoustic imaging combines the physics of optical and ultrasound imaging to provide both the high contrast and spectroscopic specificity of optical techniques and the high spatial resolution of ultrasound. It relies upon the absorption of nanosecond optical pulses to generate photoacoustic waves in absorbing structures, such as blood vessels, that propagate away to be recorded by ultrasound detectors positioned across the surface of the tissue. Measurement of the times-of-arrival of the waves and knowledge of the speed of sound allows the re-

construction of an image that represents the initial pressure distribution, which is a function of the absorbed optical energy distribution within the illuminated volume. The chromophores that provide the strongest absorption in biological tissue are oxy- and deoxyhemoglobin, and this has been exploited to obtain images of the vasculature in tumors and skin [1–3], and the brain [4,5] in small animals.

In addition, the known differences in the absorption spectra of tissue chromophores can be exploited by acquiring images at multiple excitation wavelengths. This offers the prospect of generating 3D maps of the distribution of endogenous chromophores from which physiological parameters, such as blood oxygenation and total hemoglobin concentration, can then be derived [6,7]. In addition, the distribution of

exogenous chromophores, such as systemically introduced targeted contrast agents, could also be mapped. Potential applications include studies of the oxygenation heterogeneity in vascular structures, such as those in tumors, while the ability to map and quantify targeted contrast agents may allow the study of disease processes at a molecular level [8].

An earlier study demonstrated the recovery of absolute blood oxygenation from photoacoustic spectra detected in a cuvette filled with blood using a model-based nonlinear inversion scheme [9]. The study also showed that a simple linear inversion, in which the photoacoustic signal amplitude is assumed to be proportional to the optical absorption coefficient, μ_a , allows quantitative photoacoustic blood oxygenation measurements to be made. However, this type of simple linear inversion is only valid for optically homogeneous targets. Its application is therefore restricted to very superficial blood vessels where the wavelength dependent optical attenuation by the overlaying tissue can be neglected. In order to allow measurements on deeper vessels, a number of studies have attempted to use empirical correction factors to account for the wavelength dependent tissue attenuation [10,11]. The correction factors were obtained from measurements of the wavelength dependence of the photoacoustic signal amplitude detected in a black plastic absorber (of presumably known absorption spectrum) inserted beneath the skin [3,11], or from measurements of the optical attenuation of excised tissue samples [12]. Using such correction factors, measurements of the relative hemoglobin concentration and blood oxygenation in the rat brain [12] and superficial blood vessels were made [13]. However, the disadvantage of such fixed correction factors, apart from the invasive procedures that are required to obtain them, is their strong dependence on tissue structure, composition, and physiological status. Given that these can vary significantly between different tissue types, the quantitative accuracy of these methods and their validity are likely to be limited.

To make truly quantitative photoacoustic measurements of chromophore concentrations in tissue requires accounting for the light distribution over the entire illuminated volume and the propagation of the generated photoacoustic waves. This has been demonstrated in a previous study, in which a model-based inversion scheme was used to determine chromophore concentrations from time-resolved multiwavelength photoacoustic signals measured at a single point in a tissue phantom [7]. The inversion scheme employed a forward model, which combined numerical models of the light propagation and acoustic propagation and detection, to predict photoacoustic signals as a function of arbitrary spatial distributions of different chromophores and scatterers. The use of this scheme enabled the determination not only of absolute blood oxygen saturation but also absolute concentrations of oxy- and deoxyhemoglobin.

The next step in the development of this technique is its extension to the determination of chromophore concentrations from 2D multiwavelength photoacoustic images. This is the work described in this paper, which introduces the methodology by describing the forward model (Section 3) and the inversion scheme (Section 4), and its application to the determination of chromophore concentrations from photoacoustic images acquired in tissue equivalent phantoms. The experimental methods are described in Section 5. Section 6 presents the results and discusses the accuracy and resolution of recovered parameters.

2. Quantitative Imaging Using a Model-Based Inversion Scheme

This paper describes a model-based inversion scheme in which absolute chromophore concentrations are recovered from photoacoustic images acquired at multiple excitation wavelengths. The inversion scheme incorporates a forward model, which provides multiwavelength images of the initial pressure distribution as a function of the spatial distribution of chromophore concentrations. The model is then inverted by varying the chromophore concentrations until the difference between the measured images and those predicted by the model is minimized.

In order to formulate the forward model, it is useful to consider the physical processes involved in the generation of photoacoustic images. Photoacoustic waves are produced by illuminating the tissue with nanosecond laser pulses. The propagation of the light within the tissue is dictated by the spatial distribution of the tissue chromophores and scatterers, which in turn determines the distribution of the absorbed optical energy. The absorption of the excitation pulse produces an almost instantaneous temperature rise accompanied by a local increase in pressure. This results in an initial pressure distribution that is proportional to the product of the absorbed optical energy and the Grüneisen coefficient, which provides a measure of the conversion efficiency of heat energy to stress. Broadband ultrasonic waves then propagate away from the source and are detected using ultrasound receivers positioned over the tissue surface. Using a backpropagation image reconstruction algorithm, a photoacoustic image of the initial pressure distribution can then be obtained. By obtaining images at different excitation wavelengths, a set of images is acquired where each pixel represents a spectrum of the optical absorbed energy at a specific position within the target.

To predict these images, the forward model should therefore be able to account for two physical processes: (a) the light transport in heterogeneous turbid media and (b) the generation, propagation and detection of the photoacoustic waves. To obtain estimates of the chromophore concentrations of the target, the forward model is inverted by iteratively adjusting the chromophore concentrations until the difference between the measured images and those generated by the model is minimized. In order to

ensure that the inversion produces a unique solution, prior information is included in the form of the wavelength-dependence of the optical absorption of the constituent chromophores. The key elements of this model-based inversion approach, the forward model and the inversion scheme, are described in Sections 3 and 4.

3. Photoacoustic Forward Model

Figure 1 shows a schematic of the model for the case of a single wavelength optical illumination of a turbid target containing a single absorbing object. First, a finite element diffusion-based model of light transport calculates the distribution of the absorbed optical energy as a function of the distribution of the absorption and scattering coefficients. The absorbed energy is then converted to the initial pressure distribution, which forms the input to a model of acoustic wave propagation and detection. This model is then used to calculate the photoacoustic waveforms detected at each element of a line array of ultrasound transducers. 2D photoacoustic images of the initial pressure distribution are obtained from the photoacoustic waveforms using a k -space image reconstruction algorithm. By expressing the absorption coefficient in terms of the specific absorption coefficients and concentrations of the chromophores, multiwavelength images of the initial pressure distribution can then be computed.

The light transport model is described in Subsection 3.A, the model of acoustic propagation and detection is presented in Subsection 3.B, while Subsection 3.C describes how the wavelength dependence of the constituent chromophores and scatterers was incorporated.

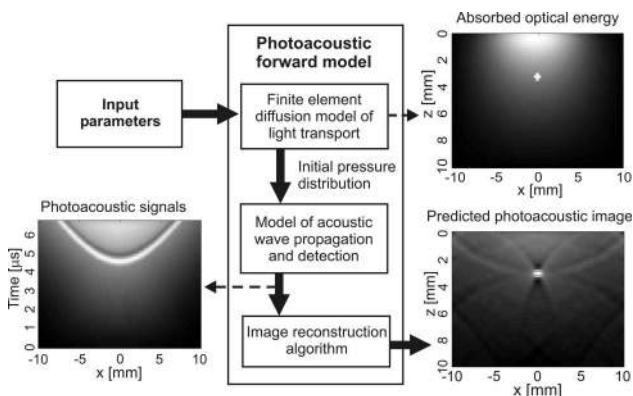


Fig. 1. Schematic of the forward model for the case of single wavelength optical illumination (center). The image on the top right shows the absorbed optical energy distribution predicted by the light transport model for a single absorber immersed in a turbid medium. The excitation light is incident from the top of the image. The image on the bottom left shows the photoacoustic signals predicted from the absorbed energy distribution using an acoustic propagation model assuming an array of acoustic detectors along the x -axis. An image reconstruction algorithm then provides the predicted photoacoustic image shown on the bottom right.

A. Model of Light Transport

A pseudo-3D finite element model of the light transport was used to calculate the absorbed energy. This involved the calculation of the absorbed energy, Q , using a 2D finite element model (FEM) of the time-independent diffusion approximation to the radiative transport equation [14]. This model can accurately represent the highly scattering nature of light transport in tissue, can be formulated for an arbitrary spatial distribution of absorbers and scatterers, and is computationally efficient enough to be used within an iterative inversion scheme. To improve the accuracy of the solution near the surface, the delta-Eddington approximation was used to describe the scattering phase function [9,15].

The wavelength dependent absorbed optical energy distribution can be expressed in 2D as

$$Q(\mathbf{r}, \lambda) = \mu_a(\mathbf{r}, \lambda) \Phi_0 \Phi(\mathbf{r}, \mu_a(\mathbf{r}, \lambda), \mu_s'(\mathbf{r}, \lambda)), \quad (1)$$

where $\mathbf{r} = \{x, z\}$ are the spatial coordinates, λ is the excitation wavelength, Φ is the internal fluence normalized to that at the surface, Φ_0 , and μ_a and μ_s' are the absorption and reduced scattering coefficients respectively. μ_a produced by n chromophores is given by

$$\mu_a(\mathbf{r}, \lambda) = \sum_{k=1}^n \alpha_k(\lambda) c_k(\mathbf{r}), \quad (2)$$

where α_k is the specific absorption coefficient and c_k is the concentration of the k th chromophore. μ_s' is given by

$$\mu_s'(\mathbf{r}, \lambda) = \mu_{sE}(\mathbf{r}, \lambda)(1 - g_E(\lambda)) \quad (3)$$

where

$$\mu_{sE}(\mathbf{r}, \lambda) = \mu_s(\mathbf{r}, \lambda)(1 - f(\lambda)) \quad (4)$$

and

$$g_E(\lambda) = \frac{g(\lambda) - f(\lambda)}{1 - f(\lambda)}, \quad (5)$$

where μ_s and g represent the scattering coefficient and scattering anisotropy, respectively. μ_{sE} and g_E are the scattering coefficient and anisotropy adjusted by f according to the delta-Eddington approximation. f , which can be expressed as a function of g [16], represents the fraction of the scattered light at shallow depths that is reintroduced into the collimated incident beam to ensure a more accurate prediction of Q near the surface [9]. The wavelength-dependent scattering coefficient is given by

$$\mu_s(\mathbf{r}, \lambda) = \alpha_{\text{scat}}(\lambda) k_{\text{scat}}(\mathbf{r}), \quad (6)$$

where $\alpha_{\text{scat}}(\lambda)$ is the wavelength-dependent scattering efficiency and $k_{\text{scat}}(\mathbf{r})$ is a scaling factor that represents the scattering strength.

Modelling the light transport in 2D implies that μ_a and μ_s are constant in y . This is reasonable since it reflects the geometry of the absorption and scattering distribution in the tissue phantom used to experimentally validate the technique as described

in Subsection 5.A. However, a 2D model implies that the light source distribution is also constant in y , which differed from the experimental setup used as this employed a circular collimated beam to irradiate the phantom surface. To account for the limited extent of the optical source in y and to create a pseudo-3D representation of the absorbed energy, $Q(\mathbf{r}, \lambda)$ was extended in the $+y$ and $-y$ direction according to a Gaussian distribution using

$$Q(\mathbf{r}', \lambda) = Q(\mathbf{r}, \lambda) e^{-\frac{2y^2}{r_b^2}}, \quad (7)$$

where $\mathbf{r}' = \{x, y, z\}$ and r_b is the e^{-2} beam radius.

In order to validate this approach, comparisons were made with a 3D Monte Carlo model [17,18]. It was found that the pseudo 3D model predicts a greater light penetration than the Monte Carlo model—this is a consequence of the assumption of a line source of infinite lateral extent that the 2D FEM implies. The difference between the output of the two models was found to be reasonably constant over the range of optical coefficients used in this study and could be corrected for by multiplying μ_s by a constant scaling factor. This factor was obtained by using both models to simulate the light distribution in a homogeneous turbid medium illuminated by a circular beam of the same diameter used in the experimental studies described in Subsection 5.A. The μ_s of the FEM was then adjusted until the depth profile at the center of the beam was the same as that provided by the 3D Monte Carlo model. The ratio of the adjusted μ_s to that used in the Monte Carlo model was then used as the scaling factor.

It should be noted that the validity of this approach rests on a number of assumptions. Firstly, the spatial distribution of optical coefficients is constant in y , thus allowing the simple conversion of the 2D absorbed energy distribution to 3D using Eq. (7). While this is a reasonable approach given the 2D nature of the tissue phantom used in this study, its validity may be compromised for targets with a more complex 3D distribution of optical coefficients. Secondly, the scaling factor was calculated for a specific illumination geometry and range of optical coefficients. In circumstances where the geometry of the target is more complex, a more general approach that employs a 3D FE light transport model may be required [19,20].

The next step is to use $Q(\mathbf{r}', \lambda)$ to calculate the initial pressure distribution p_0 and to model the propagation and detection of the photoacoustic wave from p_0 .

B. Model of the Propagation and Detection of Photoacoustic Waves

The model of acoustic propagation and detection has to account for three physical processes: first, the conversion of the optical energy density, $Q(\mathbf{r}', \lambda)$, to the initial pressure distribution; second, the propagation of the photoacoustic wave; and third, the recording of the waveforms by the transducer array. Assuming that the duration of the optical excitation is suffi-

ciently short to ensure thermal and stress confinement, the initial pressure distribution, $p_0(\mathbf{r}', \lambda)$, is given by

$$p_0(\mathbf{r}', \lambda) = \Gamma(\mathbf{r}')Q(\mathbf{r}', \lambda), \quad (8)$$

where Γ is the Grüneisen coefficient, which is a measure of the conversion efficiency of heat energy to stress. In photoacoustic imaging, Γ is usually assumed to be constant, but in this work it is assumed to be a function of chromophore concentration and is given by

$$\Gamma(\mathbf{r}') = \Gamma_{\text{H}_2\text{O}} \sum_{k=1}^n (1 + \beta_k c_k(\mathbf{r}')), \quad (9)$$

where β_k is the coefficient of the concentration-dependent change in Γ relative to that of water, $\Gamma_{\text{H}_2\text{O}}$, for the k th chromophore of concentration c_k .

$p_0(\mathbf{r}', \lambda)$ then provides the source for a 3D k -space model of acoustic propagation, which calculates the distribution of the photoacoustic wave across the whole grid as a function of time. The full details of this model can be found in [21,22]. Briefly, it requires expressing p_0 in terms of its spatial frequency components and using an exact time propagator to calculate the field at different times following the absorption of the laser pulse. The acoustic pressure, p , at position \mathbf{r}' at time t is expressed as

$$p(\mathbf{r}', t, \lambda) = \frac{1}{(2\pi)^3} \int P_0(\mathbf{k}, \lambda) \cos(\omega t) \exp(i\mathbf{k}\mathbf{r}') d^3\mathbf{k}, \quad (10)$$

where

$$\omega = c_s |\mathbf{k}| = c_s \sqrt{k_x^2 + k_y^2 + k_z^2} \quad (11)$$

where $P_0(\mathbf{k}, \lambda)$ is the 3D spatial Fourier transform of $p_0(\mathbf{r}', \lambda)$ and c_s is the speed of sound. c_s was set to that of water (1482 m s^{-1}), and the acoustic attenuation is assumed negligible. By recording the pressure as a function of time for a number of points along the x axis, a set of photoacoustic signals, $S(x, t, \lambda)$, equivalent to those detected by a line array of ultrasound transducers are obtained,

$$S(x, t, \lambda) = K \Phi_0 p'(x, t, \lambda), \quad (12)$$

where p' is the normalized detected pressure and K is the acoustic sensitivity of the detection system. The calculation of S is illustrated in Fig. 2, which shows a series of 2D images of the acoustic pressure field at the instant of optical excitation ($t_0 = 0 \mu\text{s}$) and at different times thereafter for a single absorber immersed in a scattering medium.

C. Image Reconstruction

The set of predicted signals, $S(x, t, \lambda)$, was then used to obtain an image of the normalized initial pressure distribution, $p_0'(\mathbf{r}, \lambda)$, using a 2D Fourier transform image reconstruction algorithm [23]. The predicted images, $I(\mathbf{r}, \lambda)$, can then be described using

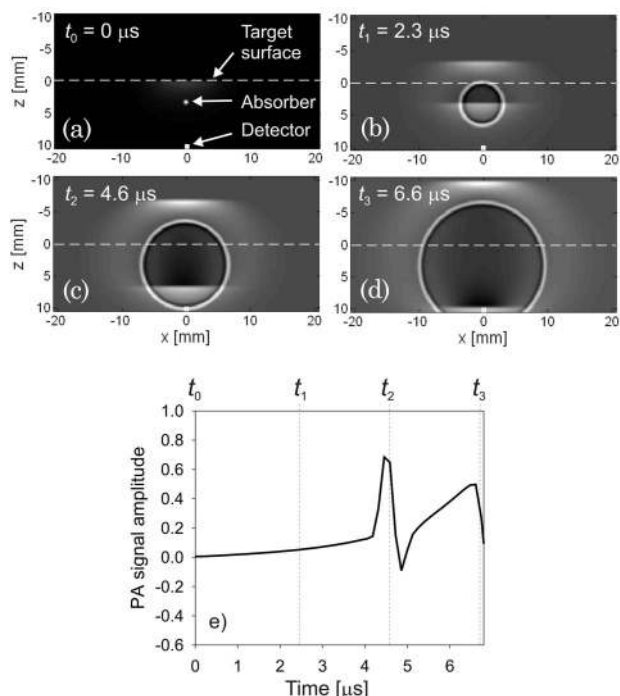


Fig. 2. Images of the acoustic pressure field calculated by the k -space model at different times after the absorption of the laser pulse. The target consists of a single absorber immersed in a scattering medium. The initial pressure distribution is shown in (a), while (b)–(d) show the propagation of the acoustic wave for subsequent times. The horizontal line indicates the target surface (e) shows the predicted photoacoustic (PA) signal, which is obtained by recording the time-dependent pressure at the element located at the center of the detector array at $\mathbf{r}' = \{0, 0, 10\}$ mm. t_2 coincides with the arrival of the wave that originated in the tube and t_3 coincides with the wave from the target surface.

$$I(\mathbf{r}, \lambda) = K'p_0'(\mathbf{r}, \lambda), \quad (13)$$

where $K' = K\Phi_0$. Equation (13) represents the complete forward model used in this study to predict multiwavelength photoacoustic images as a function of the local chromophore and scatterer concentrations. For the reconstruction, the acoustic properties were assumed homogeneous and the sound speed was set to that of water (1482 m s^{-1}).

Incorporating the reconstruction of images into the forward model was not strictly necessary since it would have been sufficient to perform the inversion by fitting the predicted time-resolved photoacoustic signals to those acquired experimentally. However, the practical implementation of the forward model required encoding the geometry of the target, which was obtained from the reconstructed images, into the model. Since it is more intuitive to work with images and since, in addition, the computational expense of the reconstruction algorithm was negligible, the image reconstruction algorithm was incorporated into the model.

D. Implementation of the Forward Model

The inversion of the forward model given by Eq. (13) would represent a general solution in the sense that

the concentrations of chromophores and scatterers could be determined for each image pixel independently. This has previously been demonstrated on simulated data [24]. However, this approach also results in a large number of variables, which can incur a substantial computational burden.

In order to reduce the scale of the inverse problem, the geometry of the target was encoded into the model. This was achieved by obtaining the locations and dimensions of absorbing features from the measured photoacoustic images and incorporating them in the grid of the FEM as discrete absorbing regions in a homogeneous background. These regions are termed the intraluminal space. The absorption coefficient of the background, which is termed the extraluminal space, was considered to be uniform. The spatial distribution of the absorption coefficient is defined as follows:

$$\mu_a(\mathbf{r}') = \begin{cases} \mu_{ai} \\ \mu_{ae} \end{cases} \quad i = 1, 2, 3 \dots n, \quad (14)$$

where μ_{ai} is the intraluminal absorption coefficient of the i th region, μ_{ae} is the absorption coefficient of the extraluminal space, and n is the total number of intraluminal regions. The division of the grid into regions resulted in a reduction in the number of variables from potentially tens of thousands to typically no more than 12. μ_s , g , and f could be described similarly but in this study were assumed to be homogeneously distributed across the entire FE grid.

In summary, the prediction of multiwavelength photoacoustic images required three steps: (1) the calculation of the absorbed energy distribution, Q , using a FEM of light transport; (2) the calculation of the initial pressure distribution, p_0 , from Q , followed by the calculation of the photoacoustic signals using the k -space model of acoustic propagation and detection, from which (3) predicted photoacoustic images are obtained using the Fourier transform image reconstruction algorithm.

4. Inversion Scheme

In Section 3, a photoacoustic forward model was described that allows the prediction of multiwavelength images. The task now is to invert this model given a set of measured multiwavelength images, that is to say, to find the values for the intra- and extraluminal chromophore concentrations and the scattering coefficient that minimize the difference between the measured data and the model output. This requires an iterative minimization scheme, whereby the model output is fitted to the measured data by varying the input parameters.

First, a vector φ containing the unknown variable model input parameters is defined as follows:

$$\varphi = \{c_{ki}, c_{ke}, k_{\text{scat}}, K\}, \quad (15)$$

where c_{ki} and c_{ke} are the intra- and extraluminal chromophore concentrations, respectively. All other input parameters, among them the spectral characteristics

of the constituent absorbers and scatterers, are regarded as prior information and are entered as fixed values. The number and position of the absorbing regions and the diameter and location of the excitation laser beam are also entered into the model as fixed parameters but are not regarded as prior information since they are obtained from the measured photoacoustic images.

Second, an inversion algorithm was employed to minimize the error function, $E(\varphi)$, by adjusting the variable input parameters contained in φ . $E(\varphi)$ is given as

$$E(\varphi) = \sum_{x,z,\lambda} (I_{\text{Data}} - I(\varphi))^2, \quad (16)$$

where I_{Data} is the measured multiwavelength image data set and I is the corresponding image data set predicted by the forward model [Eq. (13)]. The error function therefore calculates the sum of the squared difference between the measured initial pressure and that predicted by the forward model for all image pixels over all wavelengths. The minimization procedure involved the repeated calculation of predicted multiwavelength images starting from a set of initial variable input parameters contained in φ . The inversion algorithm iteratively updated φ until the sum of the squares of the difference between the model and the data was minimized. The condition for terminating the inversion was a change in E of less than that required to achieve a tolerance of 10^{-3} in the determined parameters. The values of the variable input parameters that the inversion procedure arrived at were then assumed to be the “true” values.

In addition, the uncertainty in the determined parameters, u , was calculated using

$$u = \sqrt{\text{var}(\varphi)} = \sqrt{(X' X')^{-1} \sigma^2}, \quad (17)$$

where var is the variance, X is the design matrix of the model (X' is its conjugate transpose), which contains the derivative of the model with respect to each of the input parameters in φ , and σ is the matrix of the standard deviation of I_{Data} that is obtained from repeated measurements. The values of u therefore reflect the smallest detectable change, i.e., resolution, in the determined parameters given the error in the measurement.

The inversion was executed on a computer cluster using standard Matlab functions for minimization (fminunc, BFGS quasi-Newton method) and the parallel programming toolbox. One iteration of the forward model took 90 s to complete. A typical inversion took about 6 h to complete, although it is expected that the execution time can be reduced significantly through the use of optimized and compiled code.

5. Methods

A. Experimental Setup

Figure 3 shows the experimental setup. The tissue phantom was composed of either one or four polymer

tubes (i.d. 580 μm , Morcap, Paradigm Optics), termed the “intraluminal space”. The tubes were immersed at depths between 3 and 7 mm and filled with aqueous solutions of two absorbers, copper (II)-chloride dihydrate and nickel (II)-chloride hydrate, with a maximum μ_a of 0.35 mm^{-1} and 0.55 mm^{-1} , respectively. These absorbers were used because unlike many organic dyes they were found to be photostable under nanosecond laser irradiation [25]. The tubes were submerged in an aqueous lipid emulsion (intra-lipid), termed the “extraluminal space”, which provided optical scattering. The intralipid emulsion had a lipid concentration of approximately 5%, which produced a μ_s and g of approximately 7 mm^{-1} and 0.65, respectively, at 980 nm. Small quantities of copper (II)-chloride dihydrate and nickel (II)-chloride hydrate were added to the intralipid emulsion at concentrations of 0.7 g l^{-1} and 5 g l^{-1} . This simulated the situation in tissue where the background optical absorption by hemoglobin contained in small and photoacoustically undetectable blood vessels of the capillary bed affects the signal amplitude measured in larger blood vessels.

An optical parametric oscillator (OPO) laser system provided 7 ns laser pulses between 590 nm and 980 nm at a pulse repetition rate of 10 Hz. The OPO was calibrated using a spectrometer and had a wavelength tuning accuracy of less than 1.0 nm. A hinged mirror was used to couple either the signal or idler output of the OPO into a 1.5 mm fused silica optical fiber. Homogenization of the excitation beam profile was achieved by inducing strong bends in the fiber. The fiber output was collimated onto the surface of the phantom using an achromatic lens doublet to produce an e^{-2} beam diameter of approximately 12 mm. The use of the lens doublet eliminated variations in the beam diameter caused by chromatic aberration, a typical characteristic of spherical lenses. The pulse energy incident on the phantom ranged from 4 to 30 mJ. A small portion of the OPO output was directed to a wavelength-calibrated photodiode in order to normalize the detected photoacoustic waveforms with respect to the incident pulse energy.

The acoustic waves were detected in forward mode using a photoacoustic scanning system [26] along a line of 20 mm in 0.2 mm increments. Its ultrasound sensing mechanism is based on the interferometric detection of acoustically induced changes in the optical thickness of a Fabry–Perot polymer film interferometer. The sensor was read out by scanning a focused cw interrogation beam across its surface. At each position of the scan, a photoacoustic signal was recorded. The detection bandwidth was limited to 20 MHz. At each excitation wavelength, 16 images were acquired using a digital oscilloscope for offline signal averaging. The acquisition of a complete set of multiwavelength images at eight different wavelengths involved scanning from 590 to 680 nm in 30 nm steps and from 740 to 980 nm in 80 nm steps.

Two different phantom designs, containing either a single tube or four tubes, were studied.

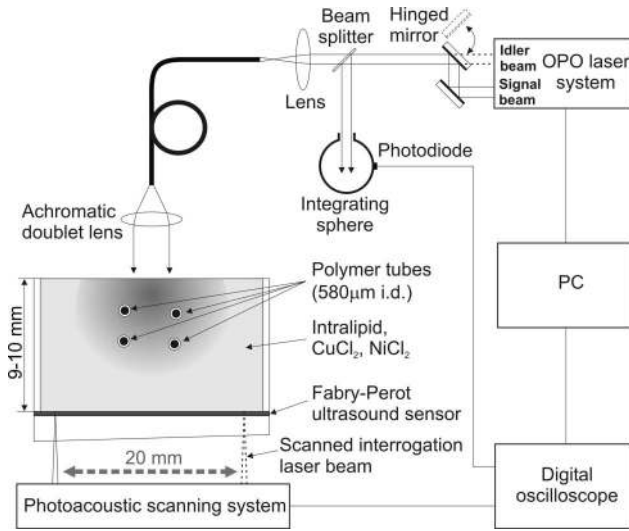


Fig. 3. Experimental setup for the acquisition of 2D photoacoustic images of a tissue phantom at multiple excitation wavelengths.

Experiments were conducted using four different compositions for the extraluminal space: (1) intralipid only, (2) intralipid with copper chloride, (3) intralipid with nickel chloride, and (4) intralipid with copper and nickel chloride. For each composition, measurements were made at different intraluminal concentration ratios of copper (II)-chloride dihydrate and nickel (II)-chloride hydrate ranging from 0 to 100% in increments of 12.5%.

B. Absorbers

The tissue phantom contained four chromophores: copper (II)-chloride dehydrate, nickel (II)-chloride hydrate, water, and lipid. Their absorption spectra are shown in Fig. 4. Copper (II)-chloride dihydrate and nickel (II)-chloride hydrate will be referred to as copper and nickel chloride for the remainder of this paper.

The tubes were filled with an aqueous solution of copper and nickel chloride. Following the nomenclature of Eqs. (2) and (14), the absorption coefficient in the i th tube is expressed as

$$\mu_{ai}(\lambda) = \alpha_{Cu}(\lambda)c_{Cu_i} + \alpha_{Ni}(\lambda)c_{Ni_i} + \alpha_{H_2O}(\lambda)c_{H_2O_i} \quad (18)$$

for $i = 1, 2, 3, \dots, n$,

where $\alpha_{Cu}(\lambda)$, $\alpha_{Ni}(\lambda)$, and $\alpha_{H_2O}(\lambda)$ are the wavelength-dependent specific absorption coefficients (units: $1 \text{ g}^{-1} \text{ mm}^{-1}$, defined using the natural log) of copper chloride, nickel chloride, and water, respectively, and c_{Cu_i} , c_{Ni_i} , and $c_{H_2O_i}$ are the corresponding intraluminal concentrations. n is the number of tubes in the phantom. The specific absorption spectra of copper chloride and nickel chloride were obtained from measurements of $\mu_a(\lambda)$ made on solutions of known concentration using a dual beam spectrometer. They are shown in Fig. 4, which illustrates that the maximum specific absorption coefficient of copper chloride is an order of magnitude greater than that of nickel chloride. This meant that a copper chloride

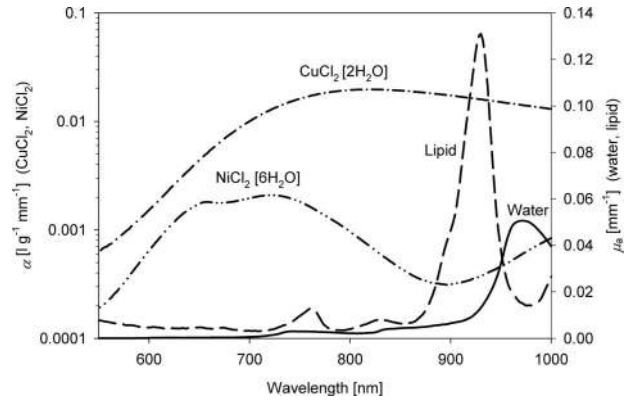


Fig. 4. Specific absorption coefficient spectra of copper (II)-chloride dihydrate ($\text{CuCl}_2 \cdot 2\text{H}_2\text{O}$) and nickel (II)-chloride hydrate ($\text{NiCl}_2 \cdot 6\text{H}_2\text{O}$) and the absorption spectra of water and lipid.

concentration of 27.7 g l^{-1} was required to obtain μ_a of 0.55 mm^{-1} and a much higher concentration of 158 g l^{-1} was required for nickel chloride to produce μ_a of 0.3 mm^{-1} . The absorption spectrum of water was taken from Ref. [27]. The absorption coefficient for the extraluminal space was defined as

$$\mu_{ae}(\lambda) = \alpha_{Cu}(\lambda)c_{Cu_e} + \alpha_{Ni}(\lambda)c_{Ni_e} + \alpha_{Lipid}(\lambda)c_{Lipid} + \alpha_{H_2O}(\lambda)c_{H_2O_e}, \quad (19)$$

where $\alpha_{Lipid}(\lambda)$ is the wavelength-dependent specific absorption coefficient of lipid, which was based on the measurements described in Ref. [28]. c_{Cu_e} , c_{Ni_e} , c_{Lipid} , and $c_{H_2O_e}$ are the extraluminal concentrations of copper and nickel chloride, lipid, and water, respectively. $c_{H_2O_i}$, c_{Lipid} , and $c_{H_2O_e}$ were considered known and entered into the forward model as fixed input parameters.

C. Scatterers

The wavelength dependence of μ_s' depends on three parameters: the scattering coefficient, the scattering anisotropy, and f , the modification factor used in the delta-Eddington approximation (Subsection 3.A). The scattering coefficient is assumed to be the same for the intra- and extraluminal space. It is assumed that the scattering coefficient is linearly related to scatterer concentration, which is a reasonable assumption given the small variations in the intralipid concentration in the phantom used. In order to obtain an accurate $\alpha_{scat}(\lambda)$, the size distribution of lipid droplets in intralipid was measured using a particle sizer (Malvern Zetasizer Nano). From this and the refractive indices of water and soy oil, $\mu_s(\lambda)$ was calculated using Mie theory, normalisation of which yielded $\alpha_{scat}(\lambda)$. In addition, Mie theory provided the wavelength dependence of the scattering anisotropy, $g(\lambda)$, and from this the wavelength dependence of $f(\lambda)$ in intralipid could be calculated based on an empirical formula ($f = 0.026094 \text{ g}^3 + 0.23597 \text{ g}^2 + 0.13572 \text{ g} + 0.60366$) as described in Ref. [16]. $g(\lambda)$, $f(\lambda)$, and $\mu_s(\lambda)$ are then used as input parameters in Eq. (1).

D. Measurement of the Grüneisen Coefficient

According to Eq. (9), the Grüneisen coefficient is dependent upon the concentration of the chromophores, which, in this study, are copper and nickel chloride. In order to determine the concentration dependence of Γ , the amplitude of photoacoustic signals produced in aqueous solutions of copper and nickel chloride was measured as a function of c_{Cu} and c_{Ni} at an excitation wavelength of 1450 nm. At this wavelength, copper and nickel chloride produce a negligible μ_a ($<0.05 \text{ mm}^{-1}$) compared to that of water (2.9 mm^{-1}) over the range of concentrations studied. Any change in the photoacoustic signal amplitude with c_{Cu} or c_{Ni} is therefore due to a change in Γ .

This allowed the coefficients β_{Cu} and β_{Ni} to be estimated, and they were found to be $5.8 \cdot 10^{-3} \text{ l g}^{-1}$ and $2.25 \cdot 10^{-3} \text{ l g}^{-1}$, respectively, which indicates an increase in Γ with concentration.

E. Comparison of the Output of the Forward Model with Measured Data

Figure 5(a) shows a measured image obtained at $\lambda = 740 \text{ nm}$ using the phantom shown in Fig. 3. The phantom comprises four tubes filled with solutions of copper and nickel chloride at different concentrations resulting in a different μ_a for each tube ranging from 0.3 mm^{-1} to 0.4 mm^{-1} . The tubes were submerged in intralipid. Figure 5(b) shows the image predicted by the forward model for the same spatial distribution of optical coefficients. The vertical and horizontal profiles shown in Figs. 5(c) and 5(d) illustrate the agreement between the model and the measured data. In particular, the forward model is shown to reproduce features that are obvious image reconstruction artifacts, such as the regions of negative initial pressure in Fig. 5(c).

6. Results

Multiwavelength images were acquired at a number of intraluminal concentrations ratios for four different compositions of the extraluminal space. From

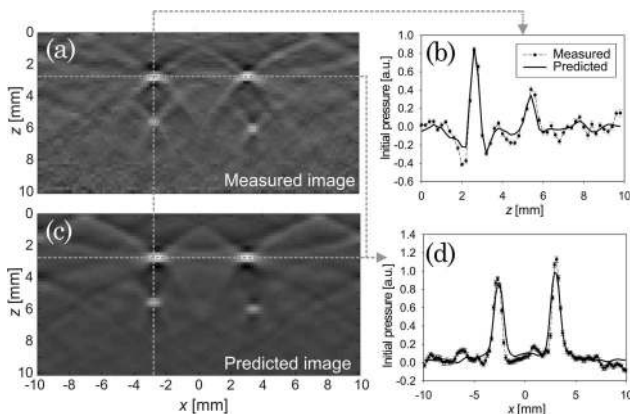


Fig. 5. Comparison of measured photoacoustic image (a) with that predicted by the model, (b) acquired at a single excitation wavelength in a phantom containing four tubes filled with solutions of copper and nickel chloride. (c) and (d) Vertical and horizontal profiles through images shown in (a) and (b), respectively.

these images, the chromophore concentrations and the scattering coefficient were determined using the inversion scheme described in Section 4. The accuracy is given by the average of the difference between the photoacoustically determined and known concentrations, while the resolution is given by Eq. (17). The presentation of the results is divided into two parts: the results obtained from phantoms containing a single tube are given in Subsection 6.A, while the results for a phantom containing four tubes are discussed in Subsection 6.B.

A. Tissue Phantom Containing a Single Tube

In this section, the results obtained from images acquired in tissue phantoms containing a single tube are presented. The tube was filled with different solutions of copper and nickel chloride, which were mixed to produce a range of concentration ratios. The tube was positioned at $x = 0 \text{ mm}$ and at a depth, z , of approximately 4 mm. The extraluminal space was filled with four different compositions of the lipid emulsion as outlined in Subsection 5.A.

1. Absolute Intraluminal Chromophore Concentrations

Figure 6 shows the absolute intraluminal concentrations of copper and nickel chloride, $c_{\text{Cu}i}$ and $c_{\text{Ni}i}$, respectively, determined using the inversion scheme for each of the compositions of the extraluminal space plotted against the known intraluminal concentration of each chromophore. Table 1 shows the accuracy and resolution values obtained from each set of measurements.

Figure 6 shows that the majority of the determined concentrations broadly agree with the known values in that the majority lie within a $\pm 15\%$ error margin and that they follow a linear relationship. However, there is a noticeable decrease in the resolution of $c_{\text{Cu}i}$ with increasing concentration as indicated by the error bars in Fig. 6(a), hence the resolution in Table 1 is provided as a range. The same is not observed for $c_{\text{Ni}i}$ [Fig. 6(b)], which shows that, in general, the resolution is independent of concentration. Furthermore, the resolutions of $c_{\text{Cu}i}$ and $c_{\text{Ni}i}$ shown in Table 1 differ by almost an order of magnitude. The resolution is related to the sensitivity of the technique to $c_{\text{Cu}i}$ and $c_{\text{Ni}i}$. This in turn is determined by the specific absorption coefficient, the maximum value of which is ten times greater for copper chloride than for nickel chloride (see Fig. 4). This means that the technique is more sensitive to $c_{\text{Cu}i}$ than $c_{\text{Ni}i}$, which explains the difference in resolution shown in Table 1.

However, the decrease in resolution with increasing $c_{\text{Cu}i}$ is counterintuitive since a higher chromophore concentration generally produces a higher μ_a , resulting in increased signal-to-noise ratios. The resolution (the smallest detectable difference in a particular parameter) depends firstly on the error in the measurement, in this case the standard deviation of each pixel in the measured image data set and, secondly, on

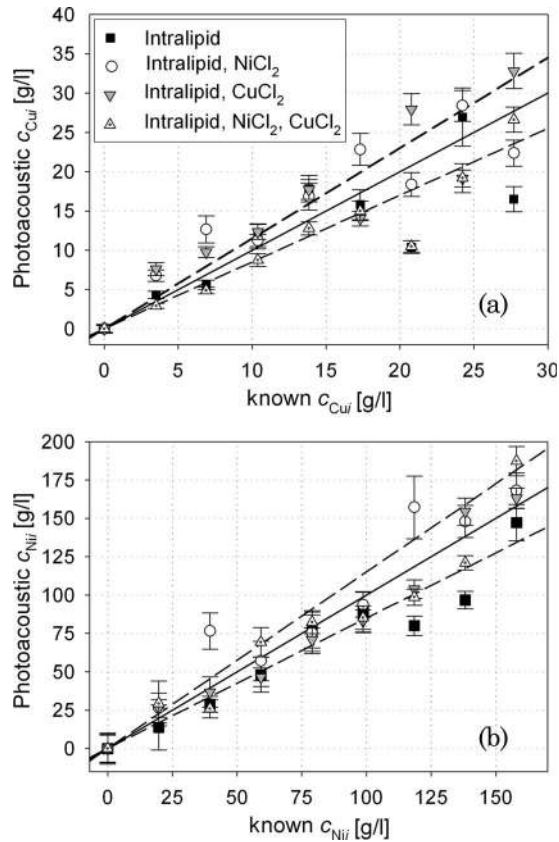


Fig. 6. Absolute intraluminal concentrations of (a) copper chloride and (b) nickel chloride determined from the measured photoacoustic images plotted against the known concentrations for four different compositions of the extraluminal space. The error bars represent the resolution of the determined values, the solid line represents the line of unity, and the dashed lines indicate the $\pm 15\%$ error margin.

the sensitivity of the measurement to the parameter in question. Since the system noise is the same for all measurements, the resolution is then primarily a function of the sensitivity to the parameter of interest, in this case c_{CuI} . If the photoacoustic signal amplitude varies linearly with concentration, the sensitivity would remain constant, and this would yield almost uniform values of resolution for all measurements. However, in scattering media, such as biological tissue or tissue phantoms, this is not the case because the intraluminal Q is nonlinearly dependent upon μ_a . This is illustrated in Fig. 7(a), which shows plots of Q calculated using the light transport model as a function of the intraluminal absorption coefficient,

μ_{ai} , and hence chromophore concentration, for different values of μ_s representative of those found in tissue [29].

It demonstrates that the nonlinearity in Q becomes more pronounced with increased scattering. This means that in a scattering medium, the sensitivity of Q to a change in μ_{ai} becomes smaller with increasing μ_{ai} . It is this change in the sensitivity that is the cause of the concentration dependence of the resolution of c_{CuI} . This effect also applies, at least in principle, to c_{NiI} yet its resolution appears to be constant. In order to explain this, the conversion of the absorbed optical energy to initial pressure needs to be considered. The conversion is, according to Eq. (8) dependent upon the Grüneisen coefficient. While it is usually assumed that Γ is spatially invariant and independent of chromophore concentration, it was found that this is not the case for copper and nickel chloride. Instead, the change in Γ was found to be a linear function of c_{CuI} and c_{NiI} (Subsection 5.D). The effect of Γ on p_0 is shown in Fig. 7(b), which was obtained by calculating p_0 as a function of the concentrations c_{NiI} and c_{CuI} , using the forward model. It shows plots for the cases of constant and concentration-dependent Γ calculated at two wavelengths where each chromophore exhibits high absorption, which for nickel chloride was 680 nm and for copper chloride 820 nm. When Γ is held constant, p_0 is simply proportional to $Q(\mu_{ai})$ and exhibits the nonlinearity associated with optical scattering similar to that shown in Fig. 7(a). The nonlinearity is somewhat more pronounced for c_{NiI} compared to c_{CuI} , which is explained by the higher μ_s in the extraluminal space at 680 nm compared to that at 820 nm. However, when Γ is a function of concentration, the nonlinearity is either strongly reduced, as is the case for c_{CuI} , or almost completely disappears, as is the case for c_{NiI} . This is due to the increase in the intraluminal Γ with increasing chromophore concentration. The concentration dependence of Γ effectively counteracts the nonlinearity caused by scattering and can, as in the case of the high concentrations of nickel chloride (maximum $c_{NiI} = 158 \text{ g l}^{-1}$), even offset it. In this case, the almost linear increase in p_0 with μ_a results in a near constant sensitivity and explains the uniform resolution of c_{NiI} shown in Table 1. By contrast, p_0 is still nonlinear for changes in c_{CuI} , which is largely due to the lower concentrations used (maximum $c_{CuI} = 27.7 \text{ g l}^{-1}$), resulting in negligible change in Γ . This in turn results in the nonuniform,

Table 1. Average Accuracy and Resolution of the Intraluminal Concentrations of Copper and Nickel Chloride Determined Using the Inversion Scheme for Different Compositions of the Extraluminal Space

Extraluminal Space Composition	Accuracy [g l^{-1}]		Resolution [g l^{-1}]	
	c_{CuI}	c_{NiI}	c_{CuI}	c_{NiI}
Intralipid	-1.7	-14.5	± 0.4 to ± 2.0	± 9.8
Intralipid, CuCl_2	1.9	-2.9	± 0.4 to ± 2.2	± 7.6
Intralipid, NiCl_2	1.6	10.1	± 0.5 to ± 3.7	± 12.0
Intralipid, CuCl_2 , NiCl_2	-2.7	-1.3	± 0.3 to ± 1.9	± 8.2

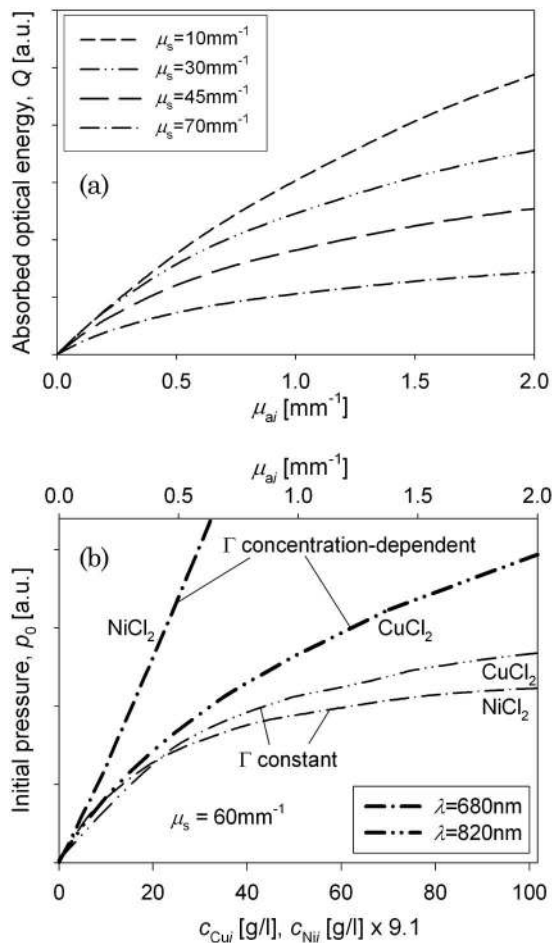


Fig. 7. Intraluminal absorbed optical energy (a), predicted using the light transport model, as a function of the intraluminal μ_{ai} for different μ_s . Figure 7(b) shows the initial pressure, p_0 , as a function of c_{Cu} and c_{Ni} (and hence μ_{ai}) in the intraluminal space for constant Grüneisen coefficient (thin lines) and concentration-dependent Grüneisen coefficient (thick lines) calculated at two wavelengths, 680 nm and 820 nm, which coincided with high values for μ_a of nickel and copper chloride.

concentration-dependent distribution of the resolution as shown in Fig. 6(a).

2. Concentration Ratio

An important application of spectroscopic photoacoustic imaging is the measurement of blood oxygenation (sO_2), which is given by the ratio of the concentration of oxyhemoglobin to the total hemoglobin concentration. By substituting the two absorbers used in this study for oxy- and deoxyhemoglobin, we can obtain the “ sO_2 equivalent” quantity R_i , thus

$$R_i = \frac{c_{Ni}}{c_{Ni} + \gamma c_{Cu}} \times 100\%, \quad (20)$$

where γ is the ratio of the nickel and copper chloride concentrations of the stock solutions from which the mixtures were prepared. γ therefore ensures that the total chromophore concentration remained constant. The ratio of the extraluminal concentrations, R_e , was calculated similarly from the determined

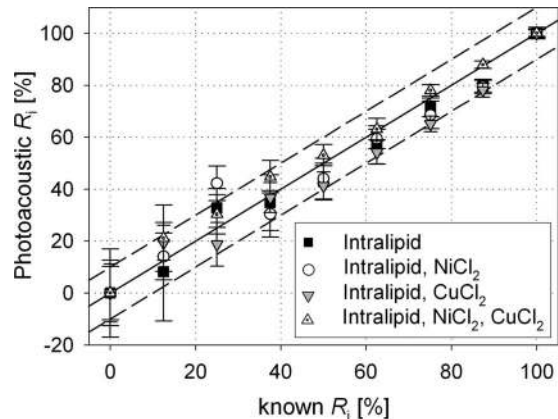


Fig. 8. Comparison of the photoacoustically determined R_i to the known values for the four compositions of the extraluminal space. The error bars represent the resolution, the solid line represents the line of unity, and the dashed lines represent the $\pm 10\%$ margin.

c_{Cu} and c_{Ni} . The results for R_i are shown in Fig. 8, and the accuracy and resolution are given in Table 2. The photoacoustically determined values increase linearly with the known concentration ratio and are generally in good quantitative agreement for all ratios with the majority of the values within $\pm 10\%$ of the known values (Fig. 8) and an average accuracy within $\pm 5\%$ (Table 2). The accuracies are again the averages of the difference between the photoacoustically determined R_i and the known values for each different composition of the extraluminal space. The resolution shown in Fig. 8 worsens towards low concentration ratios. Since the resolution of the ratios is calculated from those of c_{Cu} and c_{Ni} , its variation can be directly linked to the concentration-dependent changes in the resolution of c_{Cu} as discussed in Subsection 6.A.1.

The results shown in Fig. 8 suggest that the concentration ratio is a more robust parameter than the absolute concentrations since the determined R_i are closer to the line of unity and show less scatter than the results for c_{Cu} and c_{Ni} in Fig. 6. The determination of the absolute concentrations is dependent upon fitting the forward model simultaneously to the relative amplitudes of the spectra detected in the tube and those detected in the extraluminal space. Any error in the relative amplitudes results in errors in the determined concentrations. R_i on the other hand can in principle be determined from the shape of the spectrum alone. Errors in the absolute intraluminal concentrations, which will affect c_{Cu} and c_{Ni} equally,

Table 2. Average Accuracy and Resolution of the Photoacoustically Determined R_i for the Four Compositions of the Extraluminal Space

Extraluminal Space Composition	Accuracy [%]	Resolution [%]
Intralipid	-2.6	± 2.2 to ± 18.9
Intralipid, $CuCl_2$	-4.1	± 1.6 to ± 11.4
Intralipid, $NiCl_2$	-1.3	± 1.6 to ± 12.6
Intralipid, $CuCl_2$, $NiCl_2$	3.1	± 1.3 to ± 12.8

are therefore canceled out, which results in a more accurate determination of R_i .

3. Absolute Extraluminal Chromophore Concentrations

Figure 9 shows the extraluminal concentrations of copper and nickel chloride plotted against the intraluminal concentration ratio for the four different compositions of the extraluminal space. The known c_{Cu_e} and c_{Ni_e} are shown for comparison by the dashed lines. Table 3 shows the accuracy and resolution of the determined values.

Figure 9 illustrates that the inversion enables not only the detection of extraluminal chromophores but also the quantification of their concentration with an accuracy and resolution as shown in Table 3. It is also noticeable that the resolution of c_{Cu_e} and c_{Ni_e} is much smaller than that obtained for the intraluminal concentrations (Table 1), indicating a much greater sensitivity to the extraluminal chromophore concentrations. The reason for this may lie in the much larger number of image data points that represent the extraluminal space (typically 40,000) compared to those of the intraluminal space (80). This means that a change in the extraluminal concentrations influences a far greater number of image pixels compared to the number of pixels that are sensitive to a change in the intraluminal concentrations. This leads to higher sensitivity to extravascular chromophores, and hence a higher resolution.

The mean extraluminal concentration ratios, R_e , were calculated from the photoacoustically determined c_{Cu_e} and c_{Ni_e} and are shown in Table 4. Table 4 illustrates that the photoacoustically determined values are in good quantitative agreement with the known ratios with resolutions better than those obtained for R_i . The higher resolution is linked to the higher sensitivity in c_{Cu_e} and c_{Ni_e} discussed in Subsection 6.A.3.

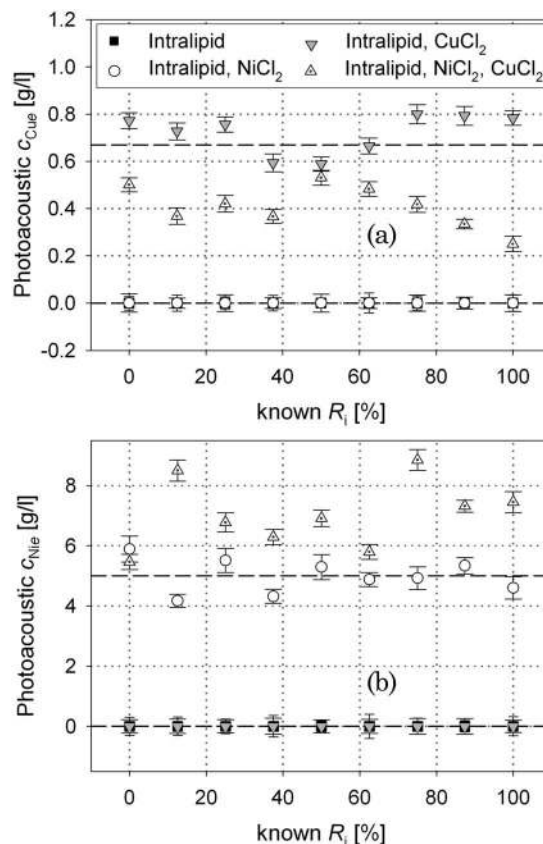


Fig. 9. Absolute extraluminal concentrations of copper chloride (a) and nickel chloride (b) plotted against the intraluminal concentration ratio, R_i , for the four compositions of the extraluminal space. The dashed lines represent the known extraluminal copper and nickel chloride concentrations of 0.7 g l^{-1} and 5 g l^{-1} , respectively, for the four compositions of the extraluminal space.

4. Scattering Coefficient

Figure 10 shows the results for the scattering coefficient at 980 nm determined using the inversion,

Table 3. Accuracy and Resolution of the Extraluminal Concentrations of Copper and Nickel Chloride Determined Using the Model-Based Inversion for the Four Different Preparations of the Extraluminal Space^a

Extraluminal Space Composition	Accuracy		Resolution	
	$c_{Cu_e} [\text{g l}^{-1}]$	$c_{Ni_e} [\text{g l}^{-1}]$	$c_{Cu_e} [\text{g l}^{-1}]$	$c_{Ni_e} [\text{g l}^{-1}]$
Intralipid	0.0	0.0	± 0.03	± 0.28
Intralipid, CuCl_2	0.0	0.0	± 0.03	± 0.23
Intralipid, NiCl_2	0.0	-0.4	± 0.03	± 0.32
Intralipid, CuCl_2 , NiCl_2	-0.3	+1.3	± 0.03	± 0.27

^aFor the experiments where copper or nickel chloride was added to intralipid, the true concentrations were 0.7 g l^{-1} and 5 g l^{-1} , respectively.

Table 4. Mean Photoacoustically Determined (PA) Extraluminal Concentrations Ratios Compared to the Known Values, Together with the Accuracy and Resolution for Three Compositions of the Extraluminal Space

Extraluminal Space Composition	Known R_e [%]	PA R_e [%]	Accuracy [%]	Resolution [%]
Intralipid, CuCl_2	0.0	0.0	0.0	± 9.0
Intralipid, NiCl_2	100.0	100.0	0.0	± 3.5
Intralipid, CuCl_2 , NiCl_2	56.7	74.9	+18.2	± 2.1

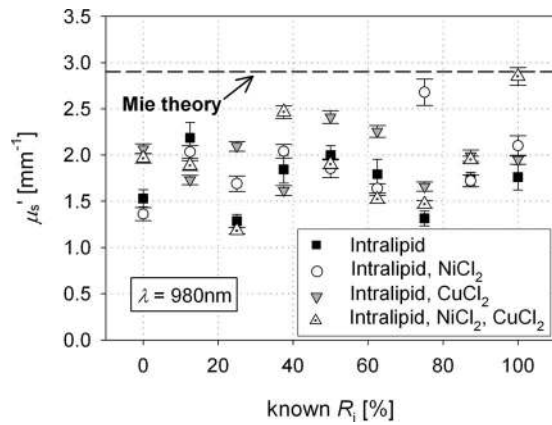


Fig. 10. Photoacoustically determined reduced scattering coefficient at 980 nm plotted against the intraluminal concentration ratios and for all four compositions of the extraluminal space. μ_s' predicted by Mie theory for intralipid is shown by the dashed line.

while the accuracy and resolution are given in Table 5. For comparison, the μ_s' predicted by Mie theory for the measured size distribution and volume fraction of the lipid droplets in intralipid and the refractive indices of soy oil and water is also shown.

The mean μ_s' for all measurements in Fig. 10 is 1.9 mm^{-1} , which is lower than the value of 2.9 mm^{-1} predicted by Mie theory. One possible source of the discrepancy is the lack of reliable data on the true refractive index mismatch between the water and lipid droplets [30]. The photoacoustically determined μ_s' are nevertheless clustered around a mean value for all the different compositions of the extraluminal space and all R_i , which is an indication of the robustness of the technique.

However, Fig. 10 also shows significant variation in the determined μ_s' , which is mainly due to the relatively low signal-to-noise ratio in the photoacoustic waveform detected in the extraluminal space, on which the determination of μ_s' relies. The error in μ_s' has a direct impact on the intra- and extraluminal concentrations determined by the inversion. This is most noticeable in the variation of c_{CuI} [Fig 6(a)].

Table 5. Photoacoustically Determined Reduced Scattering Coefficient and Its Resolution for the Four Compositions of the Extraluminal Space

Extraluminal Space Composition	μ_s' [mm^{-1}]	μ_s' resolution [mm^{-1}]
Intralipid	1.7	± 0.1
Intralipid, CuCl_2	2.0	± 0.1
Intralipid, NiCl_2	1.9	± 0.1
Intralipid, CuCl_2 , NiCl_2	1.9	± 0.1

Because the regions of high μ_a of copper chloride and water overlap (Fig. 4) between 740 nm and 980 nm, any error in μ_s' results in an inaccurate prediction of the extraluminal light attenuation, and hence c_{CuI} . By contrast, the error in μ_s' does not appear to affect the accuracy in c_{NiI} to the same extent because the μ_a of water is much lower for wavelengths shorter than 740 nm.

B. Tissue Phantom with Four Tubes

In this section, the results obtained using a tissue phantom containing four tubes are presented. An example of an image acquired at $\lambda = 740 \text{ nm}$ in such a phantom is shown in Fig. 5. Each tube was filled with a different concentration ratio of copper and nickel chloride solutions: 0% (i.e., $c_{\text{CuI}} = 25.0 \text{ g l}^{-1}$, $c_{\text{NiI}} = 0.0 \text{ g l}^{-1}$), 33%, 66%, and 100% (i.e., $c_{\text{CuI}} = 0.0 \text{ g l}^{-1}$, $c_{\text{NiI}} = 158.0 \text{ g l}^{-1}$). The extraluminal space was again variously filled with four different compositions of the intralipid emulsion as outlined in Subsection 5.A.

The inversion scheme determined the absolute c_{CuI} and c_{NiI} , and hence R_i , for each tube as shown in Fig. 11. The results in Fig. 11 show reasonable accuracy in the concentrations and R_i although there is noticeable scatter in the values for the tube marked T3. This was due to low signal-to-noise ratio as this tube was positioned furthest from the surface. It also resulted in two outliers, which were removed from the data. From the determined concentrations and R_i , the average accuracies and resolutions were calculated for all four tubes and are shown in Table 6 for the different compositions of

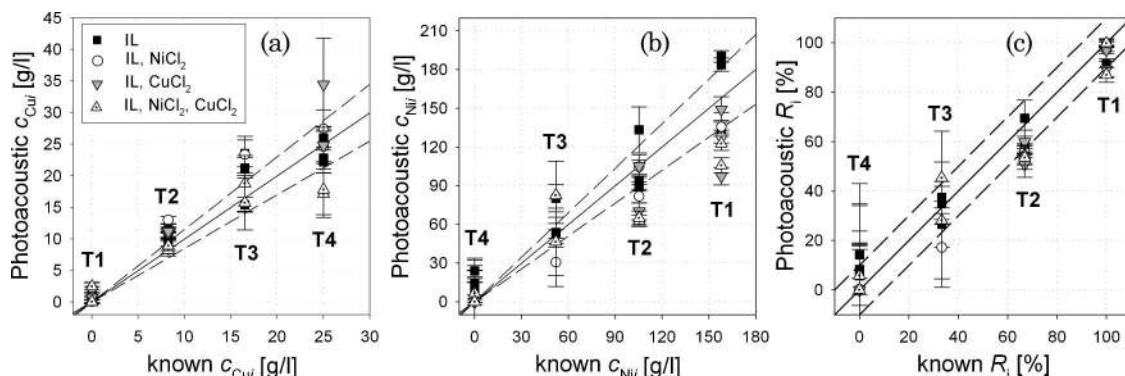


Fig. 11. Absolute intraluminal concentrations of (a) copper chloride and (b) nickel chloride determined from photoacoustic images measured in a phantom containing four tubes, which are indicated by T1, T2, T3, and T4. The intraluminal concentrations are plotted against the known concentrations for four different compositions of the extravascular space. (c) Intraluminal R_i calculated from the concentrations shown in (a) and (b). The error bars represent the resolution of the determined values, the solid line represents the line of unity, and the dashed lines indicate an error margin of $\pm 15\%$ for (a) and (b), and $\pm 10\%$ for (c).

Table 6. Mean Accuracy and Resolution of c_{Cu} , c_{Ni} and R_i Determined Photoacoustically in the Four Tubes of the Tissue Phantom, for the Four Compositions of the Extraluminal Space

Extraluminal Space Composition	Accuracy c_{Cu} [$g\ l^{-1}$]	Resolution c_{Cu} [$g\ l^{-1}$]	Accuracy c_{Ni} [$g\ l^{-1}$]	Resolution c_{Ni} [$g\ l^{-1}$]	Accuracy R_i [%]	Resolution R_i [%]
Intralipid	+1.3	± 1.4 to ± 2.9	+9.3	± 10.2	-0.1	± 0.7 to ± 18.0
Intralipid, $CuCl_2$	+2.9	± 0.6 to ± 7.4	-17.4	± 14.2	-6.0	± 3.3 to ± 34.0
Intralipid, $NiCl_2$	+2.4	± 0.3 to ± 3.0	-13.9	± 11.7	-6.1	± 1.4 to ± 23.2
Intralipid, $CuCl_2$, $NiCl_2$	-1.8	± 0.4 to ± 4.4	-17.3	± 15.0	-3.5	± 1.8 to ± 29.0

the extraluminal space. In general, the photoacoustically determined extra- and intraluminal concentrations, the concentration ratios R_i , and the scattering coefficient produced similar accuracies compared to those obtained from measurements in single tube phantom (Subsection 6.A.1). The resolution of R_i also displays a dependence on the known R_i similar to that presented in Subsection 6.A.2. This is again explained by the nonlinear response of the signal amplitude to c_{Cu} that was discussed in Subsection 6.A.2. However, the resolutions shown in Table 6 are lower than those obtained from measurements in the single tube phantom (Tables 1 and 2). This is due to the greater number of unknown variable parameters compared to the single tube measurements. Each additional variable parameter reduces the certainty, and hence resolution, in all other determined parameters.

The accuracy and resolution of c_{Cu} were $+0.1\ g\ l^{-1}$ and $\pm 0.02\ g\ l^{-1}$, and those of c_{Ni} were $+0.5\ g\ l^{-1}$ and $\pm 0.2\ g\ l^{-1}$, respectively. The mean value of the photoacoustically determined μ_s' at 980 nm was $3.0\ mm^{-1}$ with a resolution of $\pm 0.1\ mm^{-1}$. The above results demonstrate that the model-based inversion approach presented in this paper can be readily extended to any number of absorbing regions.

7. Discussion and Conclusions

A model-based inversion scheme for the recovery of absolute chromophore concentrations from multi-wavelength photoacoustic images has been developed and experimentally validated. This study has led to the following conclusions, each of which will be addressed in turn.

Firstly, a comprehensive forward model that accounts for all the physical processes involved in the generation of photoacoustic images and is formulated in three spatial dimensions is essential to obtain truly quantitative photoacoustic images. That is to say the light transport, the conversion of absorbed optical energy to initial pressure, and the propagation and detection of the photoacoustic waves must be accounted for. Although in this study a pseudo-3D light transport model provided an acceptable representation of the fluence distribution in the tissue phantom, its general application may be limited as discussed in Subsection 3.A.

Secondly, the resolution of the chromophore concentrations determined from measurements made in scattering media is due to the combination of three factors. The first is the signal-to-noise ratio, which

depends on parameters such as the sensitivity of the ultrasound transducers and the pulse energy incident on the target. The second factor is the effect of the specific absorption coefficient, α , of a chromophore on signal amplitude. Large α generally results in large changes in signal amplitude as a function of concentration, yielding high sensitivity and therefore high concentration resolution. The third factor is the nonlinear dependence of Q on chromophore concentration, and hence μ_a , in scattering media, which causes a decrease in the resolution with increasing chromophore concentration. This leads to somewhat counterintuitive conclusions since the highest resolution is achieved when, on the one hand, α of a chromophore is at a maximum while on the other its concentration, and therefore μ_a , is at a minimum. The implications of these factors can be described using the example of photoacoustic blood oxygenation measurements. An intuitive approach would be to select excitation wavelengths that coincide with the maxima of α of oxy- (HbO_2) and deoxyhemoglobin (HHb), such as those located between 530 nm and 590 nm. At physiologically realistic hemoglobin concentrations, this would result in high μ_a ($> 20\ mm^{-1}$) in blood and should therefore yield large SNR. However, unless the blood vessels are very superficial ($< 1\ mm$ depth) and located in weakly scattering tissue, the nonlinear dependence of Q on μ_a results in low resolutions of the chromophore concentrations. Instead, it is advantageous to choose excitation wavelength regions, for example around 680 nm, where the μ_a of blood is two orders of magnitude lower than at 590 nm. This would yield maximum resolution of the HHb and HbO_2 concentrations, and hence blood oxygenation.

In order to estimate the concentration resolutions of exogenous and endogenous tissue chromophores that could be achieved using the inversion scheme the forward model was used to generate simulated data using HbO_2 , HHb, and a contrast agent (Cy5) as extra- and intraluminal chromophores. The concentration resolutions for these chromophores were then calculated using the inversion scheme for the case of a single tube phantom using the experimental error of the tissue phantom measurements. The resolutions of the intravascular concentrations are $\pm 155\ \mu M$ for HbO_2 , $\pm 62\ \mu M$ for HHb, and $\pm 2.2\ \mu M$ for Cy5. By contrast, the resolutions for the extravascular concentrations are greater at $\pm 1.5\ \mu M$ for HbO_2 , $\pm 0.9\ \mu M$ for HHb, and $\pm 23\ nM$ for Cy5. These results are comparable to those of an earlier study

where a notional contrast agent was determined with a resolution of ± 63 nM [7].

Thirdly, it was found necessary to incorporate the thermomechanical properties of the tissue phantom by expressing the Grüneisen coefficient as a function of chromophore concentration. This may prove important for quantitative photoacoustic measurements in tissue where the spatial distribution of hemoglobin may vary, resulting in spatial inhomogeneities in Γ . The variation of Γ in blood may be due to hematocrit dependent changes in specific heat [31]. It is also unlikely that Γ in tissue is solely dependent upon the chromophores that provide contrast in the visible and near-infrared wavelength region. Tissue constituents that have negligible absorption in this region may also affect Γ and may need to be accounted for.

This study has demonstrated that model-based inversion schemes of the type described in this paper are well suited to the quantitative analysis of photoacoustic images acquired in biological tissue, as they can accommodate arbitrary target geometries and include any number of chromophores. By extending the methodology outlined in this paper to 3D and by using generalized inversion schemes [24], in which the absorbed energy at each pixel is expressed in terms of chromophore concentrations and scattering coefficients, 3D maps of the distribution of chromophores and scatterers may be obtained. This could provide maps of the oxy- and deoxyhemoglobin concentrations, and hence blood oxygenation, in the microvasculature. This would have many clinical and research applications, such as the study of the blood oxygenation distribution in tumors, the assessment of vascular lesions, soft tissue damage such as burns and wounds, and other superficial tissue abnormalities characterized by changes in tissue oxygenation. In addition, it may allow the mapping of the distribution of targeted contrast agents, such as those used in molecular imaging.

This work was supported by King's College London and University College London Comprehensive Cancer Imaging Centre Cancer Research UK & Engineering and Physical Sciences Research Council, in association with the Medical Research Council and Department of Health, UK.

References

1. Y. Lao, D. Xing, S. Yang, and L. Xiang, "Noninvasive photoacoustic imaging of the developing vasculature during early tumor growth," *Phys. Med. Biol.* **53**, 4203–4212 (2008).
2. E. Z. Zhang, J. G. Laufer, R. B. Pedley, and P. C. Beard, "In vivo high-resolution 3D photoacoustic imaging of superficial vascular anatomy," *Phys. Med. Biol.*, **54**, 1035–1046 (2009).
3. H. F. Zhang, K. Maslov, G. Stoica, and L. V. Wang, "Functional photoacoustic microscopy for high-resolution and noninvasive in vivo imaging," *Nat. Biotechnol.* **24**, 848–851 (2006).
4. J. Laufer, E. Zhang, G. Raivich, and P. Beard, "Three-dimensional noninvasive imaging of the vasculature in the mouse brain using a high resolution photoacoustic scanner," *Appl. Opt.* **48**, D299–D306 (2009).
5. X. Wang, Y. Pang, G. Ku, X. Xie, G. Stocia, and L. V. Wang, "Noninvasive laser-induced photoacoustic tomography for structural and functional *in vivo* imaging of the brain," *Nat. Biotechnol.* **21**, 803–806 (2003).
6. B. T. Cox, J. G. Laufer, and P. C. Beard, "The challenges for quantitative photoacoustic imaging," *Proc. SPIE* **7177**, 717713 (2009).
7. J. G. Laufer, D. Delpy, C. Elwell, and P. C. Beard, "Quantitative spatially resolved measurement of tissue chromophore concentrations using photoacoustic spectroscopy: application to the measurement of blood oxygenation and hemoglobin concentration," *Phys. Med. Biol.* **52**, 141–168 (2007).
8. A. De La Zerda, C. Zavaleta, S. Keren, S. Vaithilingam, S. Bodapati, Z. Liu, J. Levi, B. R. Smith, T. J. Ma, O. Oralkan, Z. Cheng, X. Y. Chen, H. J. Dai, B. T. Khuri-Yakub, and S. S. Gambhir, "Carbon nanotubes as photoacoustic molecular imaging agents in living mice," *Nat. Nano.* **3**, 557–562 (2008).
9. J. Laufer, C. Elwell, D. Delpy, and P. Beard, "In vitro measurements of absolute blood oxygen saturation using pulsed near-infrared photoacoustic spectroscopy: accuracy and resolution," *Phys. Med. Biol.* **50**, 4409–4428 (2005).
10. K. Maslov, H. F. Zhang, and L. V. Wang, "Effects of wavelength-dependent fluence attenuation on the noninvasive photoacoustic imaging of hemoglobin oxygen saturation in subcutaneous vasculature in vivo," *Inverse Probl.* **23**, S113–S122 (2007).
11. H. F. Zhang, K. Maslov, and L. H. V. Wang, "In vivo imaging of subcutaneous structures using functional photoacoustic microscopy," *Nat. Protoc.* **2**, 797–804 (2007).
12. X. D. Wang, X. Y. Xie, G. N. Ku, and L. H. V. Wang, "Noninvasive imaging of hemoglobin concentration and oxygenation in the rat brain using high-resolution photoacoustic tomography," *J. Biomed. Opt.* **11**, 024015 (2006).
13. H. F. Zhang, K. Maslov, M. Sivaramakrishnan, G. Stoica, and L. H. V. Wang, "Imaging of hemoglobin oxygen saturation variations in single vessels in vivo using photoacoustic microscopy," *Appl. Phys. Lett.* **90**, 053901 (2007).
14. B. T. Cox, S. R. Arridge, K. P. Köstli, and P. C. Beard, "Two-dimensional quantitative photoacoustic image reconstruction of absorption distributions in scattering media by use of a simple iterative method," *Appl. Opt.* **45**, 1866–1875 (2006).
15. B. T. Cox, S. R. Arridge, and P. C. Beard, "Quantitative photoacoustic image reconstruction for molecular imaging," *Proc. SPIE*, **6086**, 60861M (2006).
16. C. G. Chai, Y. Q. Chen, P. C. Li, and Q. M. Luo, "Improved steady-state diffusion approximation with an anisotropic point source and the delta-Eddington phase function," *Appl. Opt.* **46**, 4843–4851 (2007).
17. L. H. Wang, S. L. Jacques, and L. Q. Zheng, "CONV—convolution for responses to a finite diameter photon beam incident on multi-layered tissues," *Comp. Methods Prog. Biomed.* **54**, 141–150 (1997).
18. W. Lihong, L. J. Steven, and Z. Liqiong, "MCML—Monte Carlo modeling of light transport in multi-layered tissues," *Comp. Methods Prog. Biomed.* **47**, 131–146 (1995).
19. S. R. Arridge, M. Schweiger, M. Hiraoka, and D. T. Delpy, "A finite element approach for modelling photon transport in tissue," *Med. Phys.* **20**, 299–309 (1993).
20. M. Schweiger and S. R. Arridge, "Comparison of two- and three-dimensional reconstruction methods in optical tomography," *Appl. Opt.* **37**, 7419–7428 (1998).
21. B. T. Cox and P. C. Beard, "Fast calculation of pulsed photoacoustic fields in fluids using *k*-space methods," *J. Acoust. Soc. Am.* **117**, 3616–3627 (2005).
22. B. T. Cox, S. Kara, S. R. Arridge, and P. C. Beard, "*k*-space propagation models for acoustically heterogeneous media: Application to biomedical photoacoustics," *J. Acoust. Soc. Am.* **121**, 3453–3464 (2007).

23. K. P. Köstli and P. C. Beard, "Two-dimensional photoacoustic imaging by use of fourier-transform image reconstruction and a detector with an anisotropic response," *Appl. Opt.* **42**, 1899–1908 (2003).
24. B. T. Cox, S. R. Arridge, and P. C. Beard, "Estimating chromophore distributions from multiwavelength photoacoustic images," *J. Opt. Soc. Am. A* **26**, 443–455 (2009).
25. J. Laufer, E. Zhang, and P. Beard, "Evaluation of absorbing chromophores used in tissue phantoms for quantitative photoacoustic spectroscopy and imaging," *J. Sel. Topics Quantum Electron.* in press (2010).
26. E. Zhang, J. G. Laufer, and P. C. Beard, "Backward-mode multiwavelength photoacoustic scanner using a planar Fabry-Perot polymer film ultrasound sensor for high-resolution three-dimensional imaging of biological tissues," *Appl. Opt.* **47**, 561–577 (2008).
27. G. M. Hale and M. R. Query, "Optical constants of water in 200 nm to 200 μm wavelength region," *Appl. Opt.* **12**, 555–563 (1973).
28. R. L. P. van Veen, H. J. C. M. Sterenborg, A. Pifferi, A. Torricelli, E. Chikoidze, and R. Cubeddu, "Determination of visible near-IR absorption coefficients of mammalian fat using time- and spatially resolved diffuse reflectance and transmission spectroscopy," *J. Biomed. Opt.* **10**, 054004 (2005).
29. A. J. Welch and M. J. C. v. Gemert, *Optical-Thermal Response of Laser-Irradiated Tissue* (Plenum, 1995).
30. R. Michels, F. Foschum, and A. Kienle, "Optical properties of fat emulsions," *Opt. Express* **16**, 5907–5925 (2008).
31. A. S. T. Blake, G. W. Petley, and C. D. Deakin, "Effects of changes in packed cell volume on the specific heat capacity of blood: implications for studies measuring heat exchange in extracorporeal circuits," *Br. J. Anaesth.* **84**, 28–32 (2000).